

# Large-Eddy Simulation of the Flow Around a Simplified High Speed Train Under the Influence of a Cross-Wind

Hassan Hemida\*, Siniša Krajnović† and Lars Davidson‡

*Division of Fluid Dynamics, Department of Applied Mechanics,  
Chalmers University of Technology, SE-41296 Gothenburg, Sweden*

Large-eddy simulation (LES) was made to solve the flow around a simplified high speed train under the influence of a cross-wind. The Reynolds number of the flow was  $Re = 3 \times 10^5$  based on the height of the train and the incoming air velocity. The results are obtained at a yaw angle (the angle between the relative side wind direction and the train cruising direction) of  $90^\circ$ . Both the instantaneous and the time-averaged flows are explored. Comparison of the LES flow patterns and aerodynamic forces with experimental data was reported. It was found that the LES predicted the flow in agreement with experimental observations. Aerodynamic forces are computed and their time histories are used to find the characteristic frequencies of the flow motion around the body. The results reveal that the dominated flow motion is very small and approaches the resonance frequency of trains.

## Nomenclature

$C_p$	Local time-averaged pressure coefficient
$C_l$	Time-averaged lift force coefficient
$C_s$	Time-averaged side force coefficient, Smagorinsky constant
$D$	Height of the train model
$P_\infty$	Freestream static pressure
$U_\infty$	Freestream velocity
$St$	Strouhal number
$f$	Flow motion frequency (shedding frequency), damping function
$x$	Axial distance from the nose of the train model
$y, z$	Coordinates in the cross-sectional plane of the train model
$t^*$	Dimensionless time unit
$\Delta t$	Time step, second
$\theta$	Angle in a cross-section of the train model (see figure 5)
$\bar{u}_i$	Filtered velocity vectors
$\bar{p}$	Filtered pressure
$\tau_{ij}$	Subgrid scale stresses (SGS)
$\dot{S}_{ij}$	Resolved rate of strain
$\rho$	Air density
$y^+$	Mesh resolution in the wall normal direction
$z^+$	Mesh resolution in the streamwise direction
$x^+$	Mesh resolution in the spanwise direction

---

\* PhD student, hemida@chalmers.se

† Assistant professor, sinisa@chalmers.se

‡ Professor, lada@chalmers.se

## I. Introduction

DEVELOPMENT in train industry in the last century produced a new generation of high speed trains. These trains are characterized by a light weight to acquire a high acceleration and to reduce their energy consumption. In such case, influence of a side-wind on its stability becomes strong. The rolling and yawing moments, that result from the impact of the side and the lift forces act against the train weight and tend to derail it. Obviously, to avoid the unwanted influences of a side-wind, both the instantaneous and the time-averaged flow structures on the train surface are needed to be fully understood.

Although there have been several wind induced railway accidents in the last century, the aerodynamic influences of a side-wind on trains are not properly investigated. Many researchers studied experimentally the flow around high speed trains under the influence of a side-wind<sup>1,2,3,4,5</sup> while others used numerical techniques.<sup>6,7,8</sup> However, the available studies are still inadequate to give the complete picture of flow structures around the train in a such flow situation.

The work of Krajnović and Davidson<sup>9,10</sup> in the flow around a simplified vehicle has revealed that the time-averaged flow coherent structures distinguish themselves from the instantaneous ones. This means that the flow structures around vehicles are highly time dependent. Use of Reynolds Averaged Navier-Stokes equations (RANS) to compute the flow around vehicles provides us only with the mean information of the flow and the unsteady information are lost. Unfortunately, most of the past attempts to solve the turbulent Navier-Stokes equation used these simplified models. Khier *et.al*<sup>7</sup> have solved the time dependent Navier-Stokes equation for the flow around a simplified train model under the influence of a side-wind. They have used the time-averaged variant of Navier-Stokes equations, so called Unsteady Reynold Averaged Navier-Stokes equations (URANS). It is mentioned in that work that their chosen model represents the most accurate method among those feasible to compute flow field. The Reynolds stresses in URANS are modeled with a turbulence model. Thus the success to find a true representation of the flow is dependent on the turbulence model used. Moreover, it is difficult to define a model that can accurately represent the Reynolds stresses in the region of separated flow such as a wake behind a vehicle.<sup>11</sup>

Chiu and Squire<sup>2</sup> have studied experimentally the flow over a simplified train model in a cross-wind at different yaw angles up to  $90^\circ$ . Their results are chosen for comparison with the present numerically work. Details of this work will be considered later in the following sections.

## II. Physical model

It is hard to investigate the flow behavior around a full scale train experimentally, especially in the case of cross-wind, simply because it requires a very large wind tunnel for large yaw angles. Besides, the data obtained in the experimental studies are limited to a confined region of a line or a plane. It is also impossible to simulate the full scale train numerically since the computer resources needed are beyond the available resources nowadays. In addition, real trains are often not used for studies of the aerodynamics owing to their geometrical complexities. Instead, a simplified train model is used in both experimental and numerical studies.

In this work, the simplified model of Chiu and Squire<sup>2</sup> is chosen. The cross-sectional profile of the idealized train model was defined by the following equation

$$|y|^n + |z|^n = c^n \quad (1)$$

The model consists of two parts, a train body and a nose (see figure 1a). The train body is of a cylindrical shape with a height  $D = 125mm$  and a total length of  $9.36D$ . The profile of the cross section follows Eq. 1 in which the value of  $c = 62.5mm(D/2)$  and  $n = 5$ . The nose cross-section is given by the same equation in which  $c$  follows a semi-elliptical profile with a major diameter of  $1.28D$ , while  $n$  reduces uniformly to two at the nose tip. In this way, the cross section becomes smaller and more circular toward the nose as shown in figure 1a.

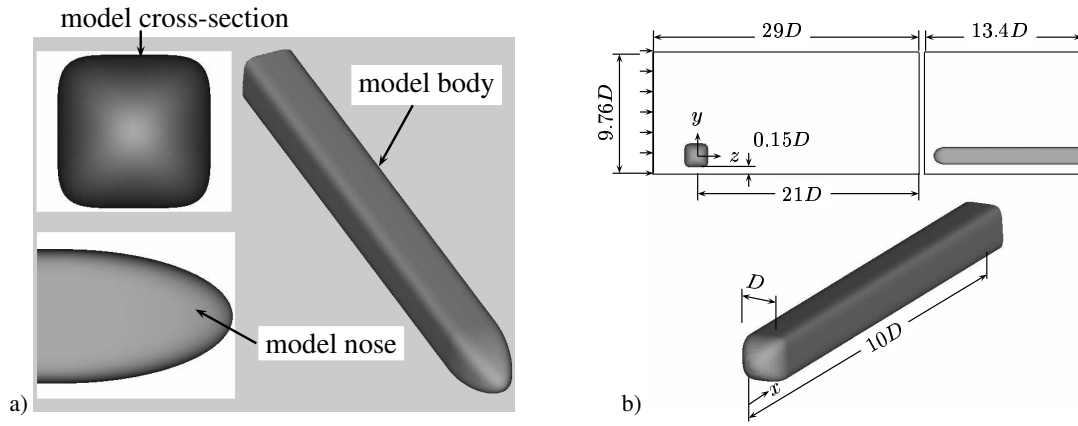


Figure 1. (a) Simplified train model shape (b) Computational domain.

### III. Large-Eddy Simulation (LES)

In LES, the large eddies are solved directly and the influences of the small scale eddies on the large scale eddies are modeled. Thus, the incompressible Navier-Stokes equations and continuity equation are filtered using an implicit spatial filter. The resulting filtered equations are:

$$\frac{\partial \bar{u}_i}{\partial t} + \frac{\partial}{\partial x_j} (\bar{u}_i \bar{u}_j) = -\frac{1}{\rho} \frac{\partial \bar{p}}{\partial x_i} + \nu \frac{\partial^2 \bar{u}_i}{\partial x_j \partial x_j} - \frac{\partial \tau_{ij}}{\partial x_j} \quad (2)$$

and,

$$\frac{\partial \bar{u}_i}{\partial x_i} = 0. \quad (3)$$

Here  $\bar{u}_i$  and  $\bar{p}$  are the resolved filtered velocity and pressure, respectively, while  $\tau_{ij} = \overline{u_i u_j} - \bar{u}_i \bar{u}_j$  are the subgrid scale (SGS) stresses. The subgrid scale stresses are the contribution of the small scales, and the unresolved stresses which are unknown and must be modeled. The Smagorinsky model is used to model the SGS stresses due to its simplicity and to reduce the computational cost as:

$$\tau_{ij} - \frac{1}{3} \delta_{ij} \tau_{kk} = -2\nu_{sgs} \bar{S}_{ij} \quad (4)$$

where  $\bar{S}_{ij}$  is the resolved rate of strain defined as:

$$\bar{S}_{ij} = \frac{1}{2} \left( \frac{\partial \bar{u}_i}{\partial x_j} + \frac{\partial \bar{u}_j}{\partial x_i} \right) \quad (5)$$

and  $\nu_{sgs}$  is the SGS viscosity defined as:

$$\nu_{sgs} = (C_s f \Delta)^2 |\bar{S}|. \quad (6)$$

Here  $|\bar{S}| = (2\bar{S}_{ij}\bar{S}_{ij})^{\frac{1}{2}}$  and  $f$  is the van Driest damping function that takes the form:

$$f = 1 - \exp\left(-\frac{y^+}{25}\right). \quad (7)$$

This damping function is used to take partially into account the effect of the wall by damping the turbulence length scale. The value of  $C_s$  in Eq. 6 is 0.1. This value has been used in a similar work for bluff-body flows and in a flow around simplified vehicles.<sup>9,10</sup> The filter width,  $\Delta$ , is taken as the cubic root of the volume of a finite volume cell.

#### IV. Why LES?

Since side-wind stability is a consequence of the flow unsteadiness, an understanding of the instantaneous flow becomes crucial in the understanding of flow around high speed trains. Thus a time-dependent method, such as Large-Eddy Simulation (LES), should be used in order to provide instantaneous information about the flow. LES has already been proved to be a reliable technique in prediction of the flow around simplified vehicles (see Refs. 9, 10). Until recently, it was impossible to predict numerically the time-dependent flow around a train model even if the flow Reynolds number is relatively low. In recent years, the increase in the computer capability have made these simulation (at moderate Reynolds numbers) possible with LES.

It is worth mentioning that complicated flow structures are developed in the wake region behind vehicles. These wake structures are dominated by large turbulent structures. Although the LES is computationally more expensive than RANS, it can provide more accurate time-averaged results and also give information on the instantaneous flow that is out of reach of RANS.

#### V. Boundary conditions and computational domain

The train model is mounted in a closed channel (wind tunnel) as shown in figure 1b. The channel has an extension of  $29D$  in the streamwise direction, a height of  $9.76D$  and a width of  $13.4D$ . It has walls at all sides except the inlet and the outlet. Similar to the experimental set-up, our train model is mounted horizontally on the wind tunnel side wall. The distance between the model and the ground is chosen to be  $0.15D$  which is typical for real trains. The model center-line position is chosen to be  $8D$  from the inlet and  $21D$  from the outlet of the numerical wind tunnel. These lengths were found sufficient in previous LES of flows around similar bodies.<sup>12</sup> The cross section of the tunnel test section, the ground clearance, and the position of the model's cross section with respect to the tunnel are identical in present LES work and the experimental set-up.

The flow enters the channel with uniform velocity constant in time. No-slip boundary conditions are used on the train surface and channel floor. Wall functions are used on the channel side walls and ceiling. Details on the implementations of the wall functions can be found in Ref. 12. Homogeneous Neumann boundary condition is used for the pressure on all the boundaries. Convective outlet boundary condition,  $\partial \bar{u}_i / \partial t + U_\infty (\partial \bar{u}_i / \partial x) = 0$  is used at the channel outlet.

#### VI. Mesh topology

In order to investigate the influence of the resolution of the near wake structure on the results and to establish numerical accuracy, two computations on two different computational grids are made: one fine mesh and one coarse mesh.

The commercial grid-generator package ICEM-CFD is used to create both the model geometry and the mesh around it. The train model is constructed using Eq. 1. Another dummy train with a height equal to  $1.15D$  is built around the model. ICEM CFD-Hexa package is employed to generate hexahedral mesh around the previously described model. An  $O$  grid is made in the belt of thickness of  $0.075D$  between the model and the dummy train. This allows making smooth mesh in all direction, see figure 2a. Figure 2a shows also another  $O$  grid of thickness  $0.5D$  (coarse mesh) and  $0.1D$  (fine mesh) that is made around the first  $O$  grid. The dummy train surface is used as a shared surface

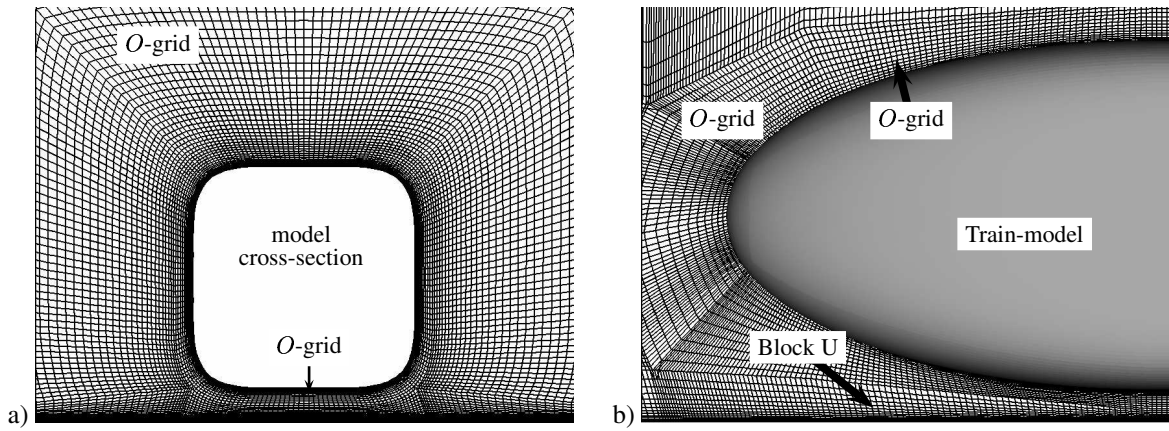


Figure 2. Coarse mesh (a) Cross-section of the mesh shows the first and the second  $O$  grids around the train model (b) Mesh shape around the train nose in the symmetry plane of the train.

between the two  $O$  grids. Figure 2b shows the mesh shape around the train nose and one block under the train (block U) which is enclosed between the second  $O$  grid and the ground board. The rest of the blocking structures was made using  $H$  grids. Hyperbolic stretching is used to make finer mesh close to the train model and coarse mesh in the regions away from the train. The total numbers of nodes are 11.5 and 8 millions for the fine and the coarse mesh, respectively.

## VII. Numerical implementations

In this work, the numerical flow predictions are carried out using an in-house finite volume developed multi-purpose package CALC-PVM for parallel computations of turbulent flow in complex multi-block domains. Large-eddy simulation (LES) equations are discretized using three-dimensional finite volume method in a collocated grid arrangement. The convective flux and the diffusion viscous plus sub-grid fluxes are approximated by central differences of second-order accuracy. The time integration is done using the Crank-Nicolson second-order scheme. The SIMPLEC algorithm is used for the pressure-velocity coupling. Additional details about this code can be found in Ref. 13.

## VIII. Spatial and temporal resolution

The equations are solved for both the coarse and fine mesh simulations starting from zero air velocity around the train model. Fully developed solution is obtained from the coarse mesh after time  $t^* = tU_\infty/D = 120$  while  $t^* = 150$  is needed to obtain fully developed turbulent flow from the fine mesh simulation. The time step is  $1.0 \times 10^{-4}$  for both of the coarse and fine mesh simulations. This value of time step gives maximum  $CFL$  number of about 0.8 and 0.75 for the coarse and fine meshes, respectively. The time-averaged flow is obtained from the simulations using  $t^* = 80$  (100,000 time steps).

Table 1. Spatial resolution for fine and coarse meshes.

Mesh	$y^+ = nu^*/\nu$	$z^+ = \Delta su^*/\nu$	$x^+ = \Delta lu^*/\nu$
Fine	1.5	50	125
Coarse	2.5	100	400

The maximum spatial resolutions of the model surface-cells expressed in the wall units are shown in Table 1 on the preceding page, where  $u^*$  is the friction velocity,  $n$  is the distance between the first node and the train surface in the wall normal direction,  $\Delta s$  is the cell width in the streamwise direction and  $\Delta l$  is the cell width in the spanwise direction.

## IX. Results

The side-wind flow is obtained around a stationary train for  $90^\circ$  yaw angle at Reynolds number of  $3 \times 10^5$  based on the height of the train and the incoming velocity. Although large yaw angles are seldom encountered in reality, it is still interesting to understand the flow structures around trains in such a flow.

Enight software package is used to visualize our LES results. Krajnović and Davidson found in their previous work that different visualization techniques are needed in different parts of the flow.<sup>12</sup> The time-averaged flow pattern on the train surface is studied using trace lines and velocity vectors projected on the train surface. Vortex cores method is used to find the vortices in the flow around the train and in the wake. Moreover, local minimum pressure and second invariant of the velocity gradient are used to analyze the coherent structures of the turbulent flow field around the train.

### A. Accuracy of the results and validation

In this Section, the accuracy of the results is investigated by two ways: mesh dependency and results verification by performing comparison with the available experimental results.

#### 1. Mesh dependency

Mesh dependency is investigated by performing two simulation with different number of nodes. The coarse and the fine meshes contain 8.5 and 11.5 million nodes, respectively. The two simulations give the same flow patterns on the model surface. Figure 3a shows the time histories of the side force coefficient  $C_s$  obtained from the fine mesh calculation that represents the force on the model in the streamwise direction while figure 3b represents the time history of the lift force coefficient  $C_l$  for the same mesh. Figure 4a and figure 4b show the same force coefficients obtained from the coarse mesh. These coefficients are defined as:

$$C_s = \frac{S}{\frac{1}{2}\rho U_\infty^2 A_z} \quad (8)$$

and

$$C_l = \frac{L}{\frac{1}{2}\rho U_\infty^2 A_y} \quad (9)$$

where  $S$  and  $L$  are time-averaged side and lift forces respectively,  $U_\infty$  is the inlet channel velocity,  $A_z$  is the train projection area in the streamwise  $z$ -direction and  $A_y$  is the train projection area in the  $y$ -direction. The side and lift forces are calculated by the integration of the averaged surface pressure in the  $z$  and  $y$  directions, respectively. The time-averaged values of these coefficients are shown in Table 2. Figure 5 shows the local pressure coefficient  $C_p$  for the fine and coarse mesh simulations as well as the experimental one at  $x/D = 6.5$ . This coefficient is defined as:

$$C_p = \frac{\langle p \rangle - p_\infty}{\frac{1}{2}\rho U_\infty^2} \quad (10)$$

where  $\langle \cdot \rangle$  denotes time averaging,  $p_\infty$  is the reference pressure, which is chosen to be the pressure at a point in the top corner of the channel inlet. The position of the reference pressure point is chosen to be far away from the model.

The two simulations give the same pressure distribution trend but a small difference is observed on the bottom-side face where lower pressure is obtained from the coarse mesh simulation. This difference in the pressure makes the coarse mesh lift force coefficient lower than that obtained from the fine mesh simulation. On the other side, same pressure values are obtained on the stream-wise face while slightly lower pressure is obtained in the lee-side face in case of coarse mesh simulation. This makes the coarse mesh side force coefficient  $C_s$  high compared to that obtained from the fine mesh simulation.

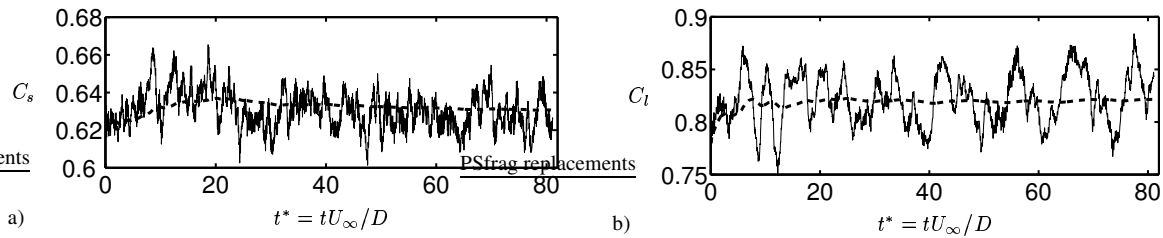


Figure 3. Time history of the force coefficients obtained from the fine mesh (a) side force coefficient (b) lift force coefficient. The dashed line is the time-averaged values of these forces.

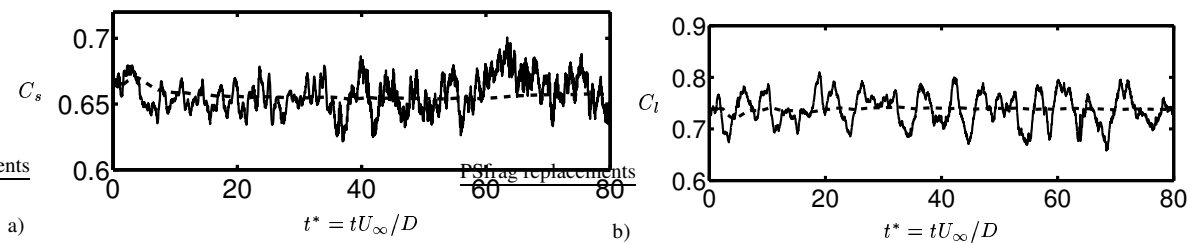


Figure 4. Time history of the force coefficients obtained from the coarse mesh (a) side force coefficient (b) lift force coefficient. The dashed line is the time-averaged values of these forces.

Table 2. Time-averaged LES force coefficients.

Mesh	$C_s$	$C_l$
Fine	0.63	0.82
Coarse	0.655	0.75

## 2. Verification with experimental data

In order to validate the LES results, extensive comparisons are performed between the fine mesh results and the available experimental results from 2 and 14 that have been collected on the same model at the same Reynolds number. Figure 5 shows that the time-averaged pressure distribution obtained from both the fine and the coarse meshes are in a good agreement with the experimental one. A slight difference is noticed on the bottom-side face where higher pressure resulted from the LES.

Figure 6 shows the LES surface flow patterns while figure 7 shows the surface oil flow patterns on the train model (taken from 2). Comparison between figure 6 and figure 7 shows that there is a good agreement on all the faces except on the roof-side face where small separation bubble is found in the LES. Figure 6a shows the flow pattern on the

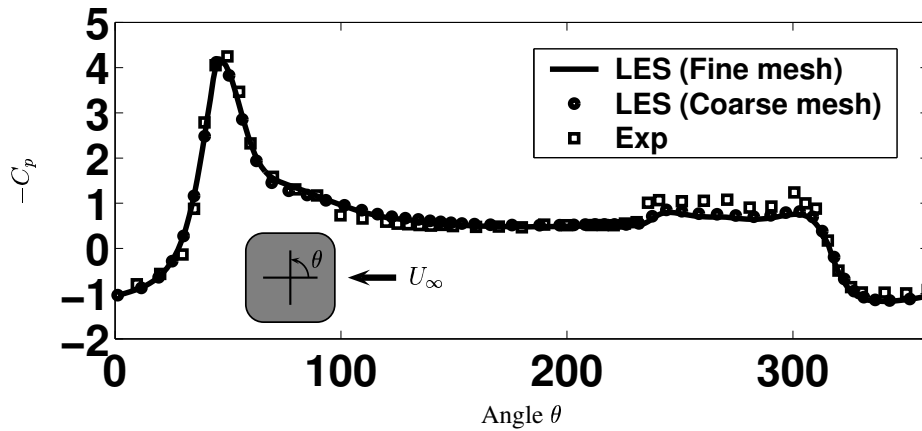


Figure 5. Time-averaged local surface pressure coefficient  $C_p$  at  $x/D = 6.5$ .

stream-wise face. Stagnation line  $St_1$  appears at a distance  $0.35D$  from the bottom-side face. The same stagnation line is found in the oil-film visualization as shown in figure 7a. A good agreement is found between LES results and experimental results on the bottom-side face as shown in figure 6d and figure 7d. The flow retains fully attached to the surface until it separates in the separation line  $S_3$ .

On the roof-side face, the LES flow pattern shows region of separation and attachment. The flow separates at line  $S_1$  and reattaches at line  $A_1$  as shown in figure 6b. Figure 8a zooms in region A in figure 6b where the separation on the roof of the model starts at approximately  $x/D \approx 3$ . The separated flow attaches again to the model surface after the re-attachment line  $A_1$  and then separates at the separation line  $S_2$  in the wake flow. The oil-flow visualization does not show separation line  $S_1$  and re-attachment line  $A_1$  but shows the separation line  $S_2$  (see figure 7b). To retain this fully attached flow in the experiment, a trip wire is attached to the roof-side windward edge since attached flow appears to correspond to the flow over full scale trains.

The vortex sheets that shed from the underside and roof of the train are rolled up to form two big bubbles which dominate the lee-side flow field. Figure 6c shows the surface flow pattern on the lee-side of the model. We find that the flow moves up toward the train roof in the upper half of the lee-side face without separation. On the lower half of the lee-side face, the flow moves down toward the bottom-side face. It separates in the bottomward edge to form a very small separation bubble. The separation starts at the separation line  $S_4$  as shown in figure 6c. Figure 8b zooms in the region B in figure 6d where the flow separates at  $S_4$  and attaches again after the reattachment line  $A_2$  (see figure 8b).

Figure 9 shows the LES and experimental surface flow pattern on both bottom-side and lee-side faces. Both the LES results (left figure) and the schematic representation of the oil-flow visualization (right figure) show a small separation bubble that starts axially at  $x/D \approx 2.5$  and stretches along the train length.

The surface flow pattern on the groundboard obtained from our LES is compared with the experimental oil-film visualization in figure 10. Good agreement is found between LES and oil-flow visualization since two separation lines,  $S_5$  and  $S_6$ , and one attachment line,  $A_3$ , are shown in both the LES and the experiment in the same position on the groundboard (see figure 10).

It is worth mentioning that, in our LES, the flow retains fully attached to the groundboard in the wind tunnel before it reaches the model, exactly the same as the oil-flow visualization.

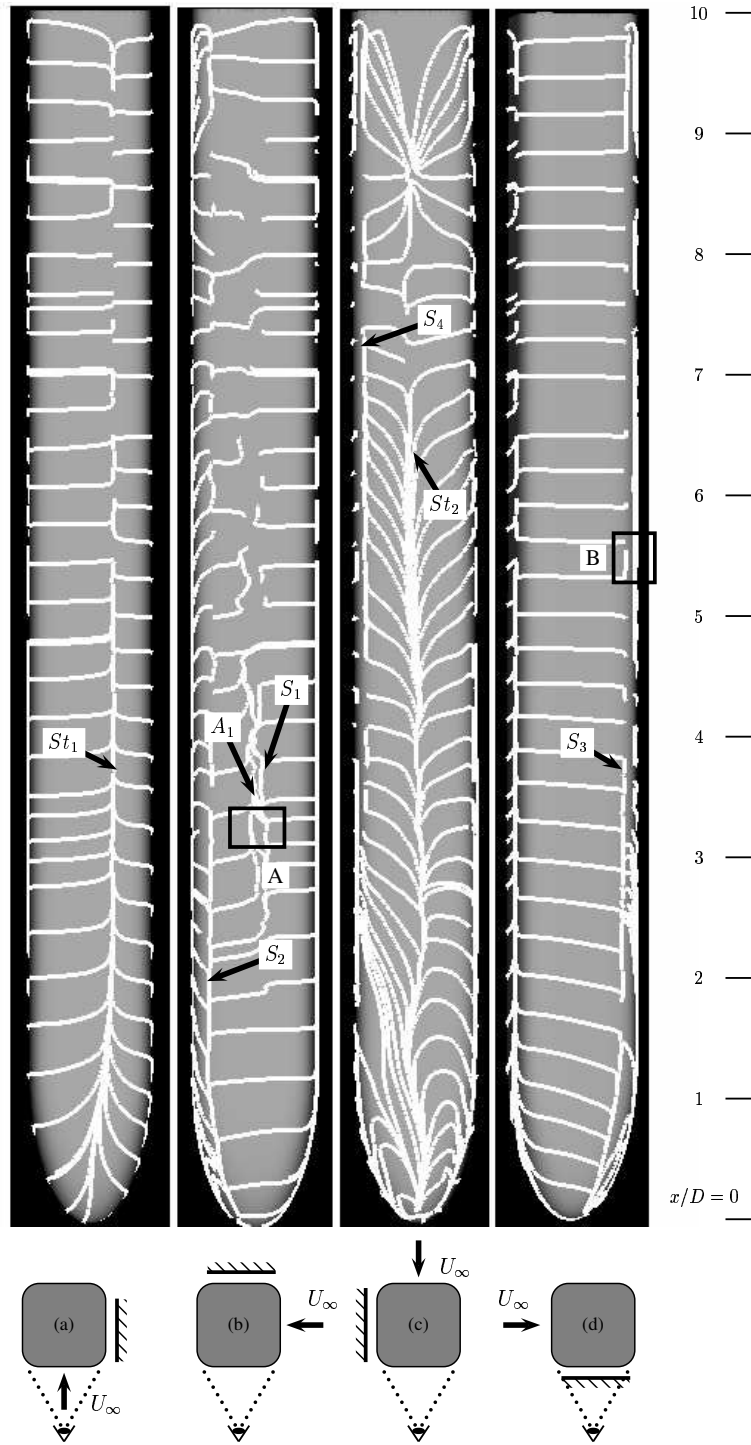


Figure 6. Time-averaged trace lines projected on the surface of the train body (fine mesh).

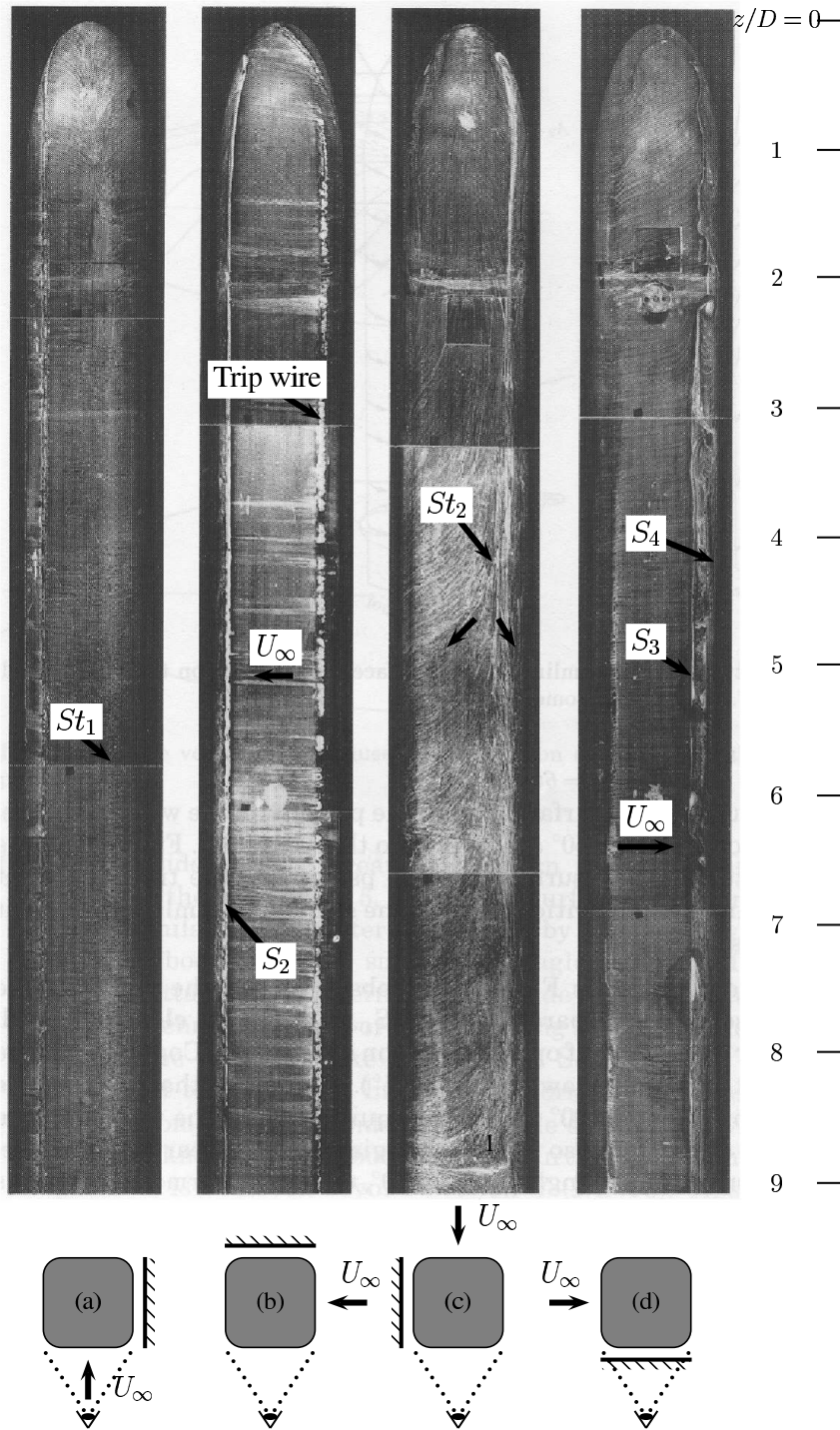


Figure 7. Oil-flow visualization on the train surface (Taken from Ref. 2 with permission from Elsevier).

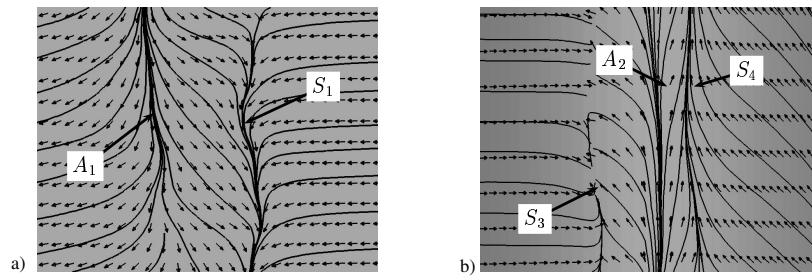


Figure 8. (a) Zoom of region A in figure 6 shows the separation on the roof-side (b) Zoom of region B in figure 6 shows the small separating region in the downward edge on the lee-side.

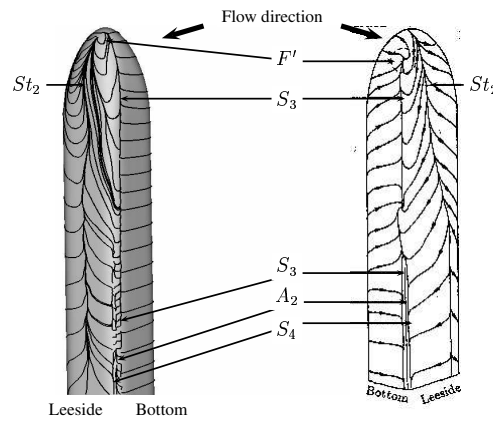


Figure 9. Surface flow pattern on the lee-side and bottom-side face. left: LES flow pattern; right: experimental flow pattern (Taken from Ref. 2 with permission from Elsevier).

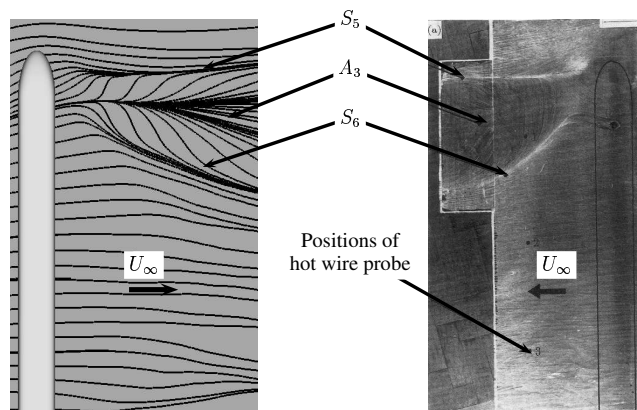


Figure 10. Groundboard flow pattern. left: LES flow pattern; right: experimental flow pattern (Taken from Ref. 2 with permission from Elsevier).

## B. Flow structures

In this Section the time-average flow around the train and in the wake is analyzed. All the results presented in this Section are from the fine mesh computation unless otherwise stated.

### 1. Separation at the top face

The effect of Reynolds number on the separation on the roof-side is investigated by Copley.<sup>3</sup> It is demonstrated in that work that there is a direct relation between the Reynolds number and the separation bubble size on the roof-side. At low Reynolds numbers, the flow separates from the roof-side windward edge, and does not reattach. If the Reynolds number is increased, at some critical Reynolds number, the flow reattaches forming a separation bubble. For higher Reynolds number, this bubble is suppressed and the flow over the roof-side is fully attached.

The magnitude of the actual Reynolds number over a real train is of the order of  $10^7$  which is impossible to simulate using LES owing to resolution requirements. Since the chosen Reynolds number in the experimental work is  $3 \times 10^5$ , which is at least 30 times lower than the full scale Reynolds number, a trip wire is attached to the windward edge at the roof-side to simulate the same flow pattern as in the case of a real train. The

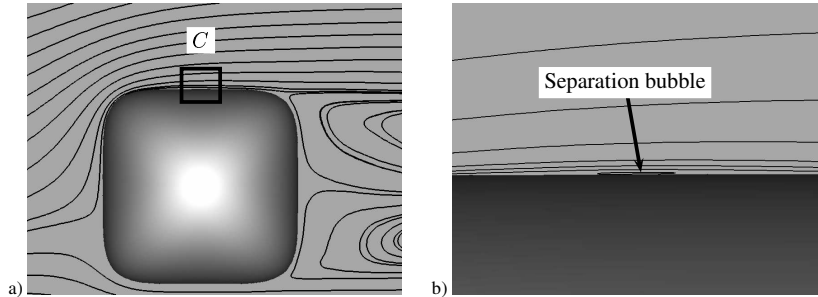


**Figure 11.** a) Time-averaged streamlines projected onto a plane  $x/D = 4$  show the separation bubble in the roof-side face. b) Zoom of region  $C$  in figure 11a

LES Reynolds number is the same as the experimental one but it is rather difficult to simulate the trip wire in the windward roof-side. Therefore, a separation is expected on the roof-side face in our LES.

Figure 11 shows time-averaged streamlines projected to a plane perpendicular to the train length at a distance ( $x/D = 4$ ) from the nose. Figure 11b zooms in region  $C$  in figure 11a. It could be demonstrated from figure 11b that the separation bubble is very small and thin in both  $z$  and  $y$  direction compare to the train height and it could be demonstrated also from figure 6b that it does not grow in the direction of train length. Different pictures from the instantaneous flow similar to Figure 11 show that this separation bubble is unstable i.e it disappears and returns back with time which makes the flow highly unsteady (these pictures are not shown here). Consequently, the surface flow pattern on the roof-side face is not uniform as shown in figure 6b.

### 2. Wake flow

The vortex sheets that shed from the underside and the roof of the train are rolled up to form two big bubbles which dominate the lee-side flow field. Figure 12a shows vortex cores that appear in the flow while Fig 12b shows an isosurface of the time-averaged static pressure in the wake flow ( $p = -0.2$ ).

The vortices that appear in the flow field in figure 12a can be described as follows:

- (1) Vortex  $V_{c5}$  appears due to the separation on the roof-side flow.
- (2) Vortex  $V_{c2}$  originates from a focus very close to the train nose (floor side).
- (3) Vortex  $V_{c3}$  that starts on the train nose (roof-side).
- (4) Vortices  $V_{c1}$  and  $V_{c4}$  have a fixed position in the wake and stretch along the train length. They start directly after vortices  $V_{c2}$  and  $V_{c3}$  turn their direction toward the wake flow.
- (5) The small vortex  $V_{c6}$  at the bottom edge of the train lee-side face.

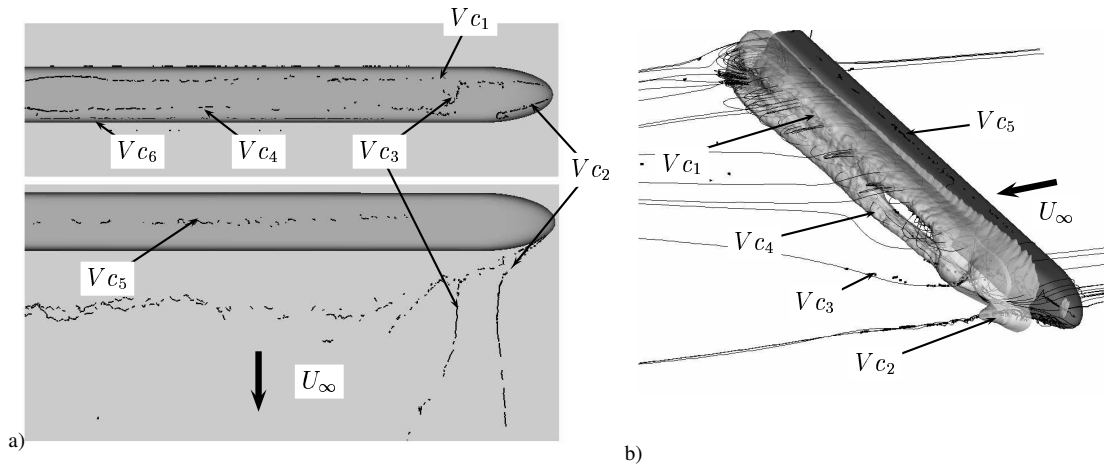


**Figure 12. Time-averaged flow structures (a) Vortex cores in the wake flow. upper figure: view from the exit toward the train; lower figure: view from the roof toward the train. (b) The isosurface of the time-averaged static pressure in the wake flow ( $p = -0.2$ ).**

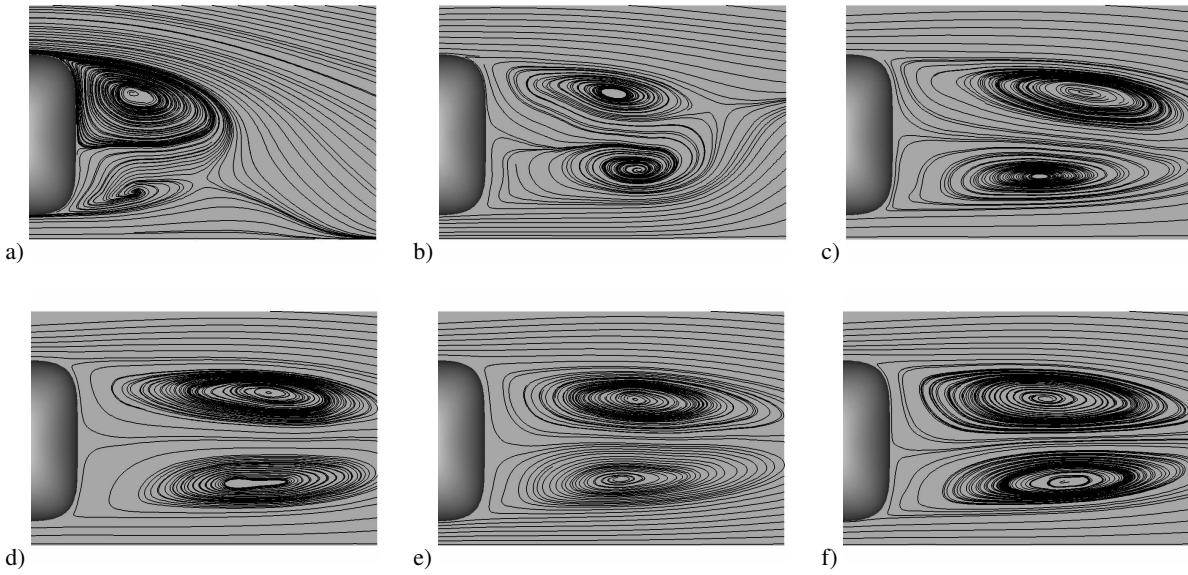


**Figure 13. Time-averaged streamlines showing the variation of the two wake vortices projected onto planes (a)  $x/D = 1.5$ , (b)  $x/D = 2.5$ , (c)  $x/D = 3.5$ , (d)  $x/D = 4.5$ , (e)  $x/D = 6$ , (f)  $x/D = 8$ .**

Figure 12b shows the same vortices in the flow field using isosurface of the local pressure minimum. Formation of the wake vortices  $Vc_1$  and  $Vc_4$  is shown in figure 13 through streamlines pattern plotted at different cross sections. This figure demonstrates that after  $x/D \approx 3.5$  the vortices are fixed in the  $z - y$  plane at approximately one train height downstream the model. The width of the vortices, in the streamwise direction, is about  $2D$  and their height is about  $0.5D$ .

### C. Surface pressure distribution

The time-averaged pressure distribution is used to calculate the local pressure coefficient  $C_p$  at different positions of the train length. Comparison of  $C_p$  values from our LES with the experimental data of Chiu<sup>14</sup> is shown in figure 14. The surface pressure distribution does not change much along the train length except in the small region close to the nose ( $x/D < 1.5$ ). Figure 14 shows that the profile does not change at all after  $z/D \approx 3.5$  in agreement with the experimental data.

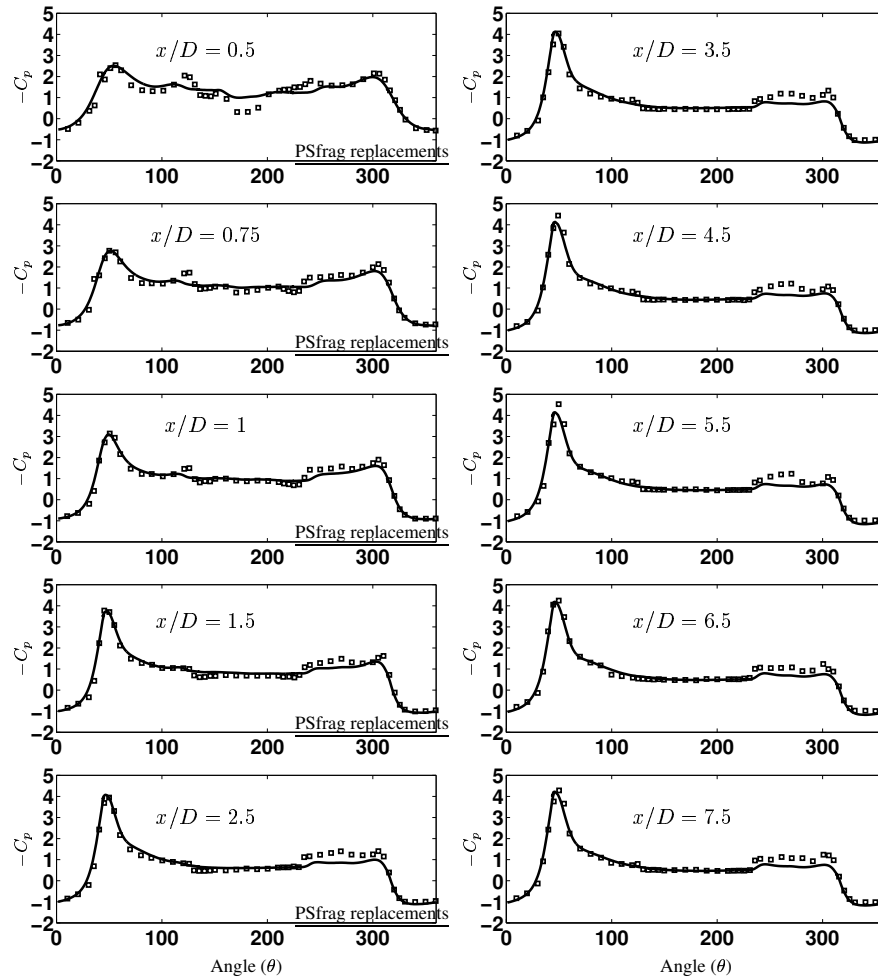


Figure 14. Comparison of the surface pressure distributions along the train length at positions: (solid line) LES; (Symbols) experiment from Chiu.<sup>14</sup>

### D. Instantaneous flow

The force coefficients  $C_s$  and  $C_l$  are saved at each time step and their time histories are used to calculate the impact frequency on the train surface. The instantaneous data covering 260 time steps ( $t^* = 1.2$ ) were saved and used to study the temporal coherent structures around the body. Below we present the result of this study.

## 1. Aerodynamic forces

The time history for side force and lift force coefficients are shown in figure 3a and figure 3b. The time-averaged values of these coefficients are presented in Table 2. The peak value for the side force coefficient is 0.66 while the minimum value is 0.6. On the other side, the maximum and minimum values for the lift force coefficient are 0.87 and 0.75, respectively. The time history of these coefficients is paid special attention. Fourier transform is used to resolve their dominating frequencies, that represent the side-wind induced forces frequencies. Figure 15a and 15b show the autopower spectra of the time varying signal  $C_s$  and  $C_l$ , respectively, against Strouhal number  $St = fD/U_\infty$ , where  $f$  is the time-varying frequency of  $C_s$  and  $C_l$ . Three dominating peaks are found in the Fourier transform of  $C_s$  at  $St = 0.07, 0.2$  and  $0.3$ . On the other side, three different peaks are founded in the Fourier transform of  $C_l$  at  $St = 0.1, 0.24$  and  $0.3$ . The most dominating  $St$  for the side force is 0.07 while the most dominating  $St$  for the lift force is 0.1. The danger associated with these frequencies is that they are very small and they approach the resonance frequencies of the real high speed trains which are corresponding to Strouhal number between 0.04 and 1.2.

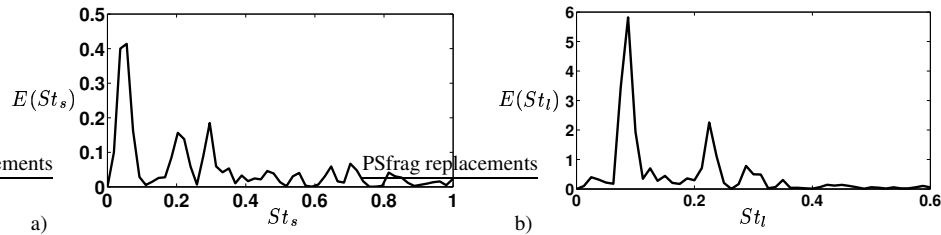


**Figure 15.** Autopower spectra  $E(St) = F(St)\bar{F}(St)$  of the time-varying force coefficients, where  $F(St)$  is the Fourier transform of the time-varying signal and  $\bar{F}(St)$  is the complex conjugate of  $F(St)$ . (a) and (b) are the autopower spectra of  $C_s$  and  $C_l$ , respectively, drawn against Strouhal number  $St = fD/U_\infty$  where  $f$  is the forces time-varying frequency

## 2. Temporal evaluation of coherent structures

The isosurface of the instantaneous second invariant of the velocity gradient  $Q = -1/2\partial u_i/\partial x_j\partial u_j/\partial x_i$  and the isosurface of the instantaneous pressure are used to study the temporal evolution of the coherent structures around the body. Figures 16a-c, show the isosurface of the instantaneous pressure at different three time steps with a time difference in between equal to  $t^* = 0.12$ . The value for the pressure used is  $p = -0.19$ . On the other side, figures 16a'-c', show the isosurface of the instantaneous second invariant of the velocity gradient at the same three times ( $Q = 7000$ ). Elongated coherent structures that are extended in the spanwise direction are formed at the windward edge on the roof-side face as shown in figure 16. Many vortices are born in that region and convected downstream. The small convected vortices merge with each other forming slightly larger vortices. Figure 16a and figure 16a' show three different vortices  $\lambda_1, \lambda_2$  and  $\lambda_3$  at time  $t^* = 0$ . After time  $t^* = 0.12$ , the vortices  $\lambda_2$  and  $\lambda_3$  are convected downstream and their middle part is lifted from the surface as shown in figure 16.b and figure 16b'. Their legs are still attached to the surface to form hairpin-like vortices. At the same time vortex  $\lambda_1$  is destroyed and only small portion of it continues downstream. After time  $t^* = 0.24$  as shown in figure 16c and figure 16c' the three vortices are destroyed and convected downstream while other vortices are formed at the windward edge. This process of formation, attaching and detaching of the vortices leaves disturbance in the surface pressure. The pressure fluctuation due to this process contributes on the time varying values of the forces around the train.

## X. Conclusion

Although the flows around trains are highly unsteady, the available knowledge about such flows are mainly that of the resulting time-averaged flow. The experimental information is limited and they do not provide us with the complete picture of the flow field. Large eddy simulation is used to establish both instantaneous and time-averaged pictures of

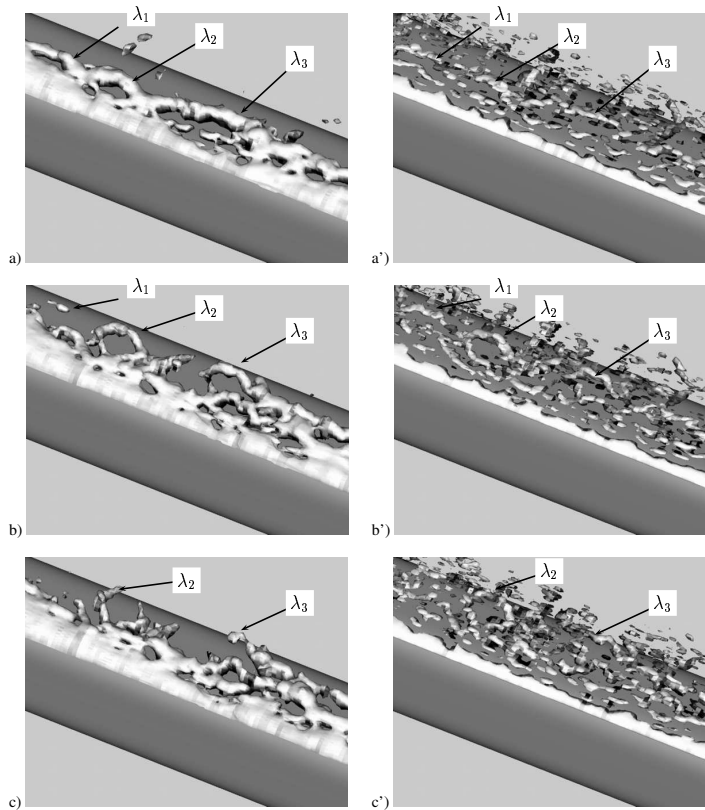


**Figure 16. Temporal evolution of the coherent structures in the region between  $x/D = 3$  and  $x/D = 6$ . (a), (b) and (c) show the isosurface of the instantaneous static pressure,  $p = -0.19$ , at three different times. (a'), (b') and (c') show the isosurface of the instantaneous second invariant of the velocity gradient  $Q = 7000$ . The time difference between two successive pictures is  $t^* = 0.12$ .**

the flow around the simplified high speed train. Two different computational grids are used. Already our coarse mesh containing 8 million nodes is adequate to get results that agree well with experiments. The LES results using fine mesh of 11.5 million nodes are compared with the experimental data and good agreement is obtained. From the LES results, the general features of the flow show the following:

- (1) The three-dimensional effect of the nose on the streamwise, roof-side and bottom surface streamline patterns are confined to the region very close to the nose. On the other side, its effect on the lee-side flow pattern is extended to a region of  $z/D \approx 3$  from the nose where axial flow is noticed.
- (2) Separation bubble appeared at the middle of the roof-side face at the simulated Reynolds number ( $3 \times 10^5$ ). To correctly simulate the flow around real trains, either the Reynolds number should be increased or trip wire should be used in the windward edge as in the experiment.
- (3) Attached flow is observed on the groundboard upstream of the model. On the other side, two separation lines and one reattachment line are found on the groundboard downstream of the model. The numerical results obtained on the groundboard are in good agreement with experimental observations.
- (4) LES gives time-averaged surface pressure distribution in good agreement with experiments over streamwise, lee-side and roof-side surface of the model. Higher surface pressure is obtained on the bottom-side surface.
- (5) Axial flow is obtained in the lee-side face close to the train nose due to the existence of two strong vortices in the wake that starts on the train nose.

- (6) Two big spanwise bubbles are obtained in the wake. They are elongated in the direction of the train length. The position of their cores is  $1D$  downstream from the model. Their size is constant after  $z/D \approx 2.5$  with height of approximately  $0.5D$  and width of approximately  $2D$ .
- (7) The time-dependent flow is used to show very small structures close to the wall which are not found in the time-averaged flow. The evolution of the coherent structures is explained and their influence on the surface forces is revealed.
- (8) The time history of the force coefficients is used to find the dominating frequencies of the flow around the train. Three dominating peaks are found in the Fourier transform of side-force coefficient  $C_s$  at the Strouhal numbers  $St = 0.07, 0.2$  and  $0.3$ . On the other side, three peaks are found in the Fourier transform of lift-force coefficient  $C_l$  in the range of  $0.1 < St < 0.3$ . The flow frequencies corresponding to these coefficients are very small and they approach the resonance frequencies of the real high speed trains.

The knowledge gained in this work will hopefully help engineers to understand better the flow around trains under the influence of side wind and hence improve their ability to withstand the influences of side wind.

## XI. Acknowledgment

This work was supported by the Swedish Agency for Innovation System (VINNOVA), Bombardier Transportation, and Scania. Computer time on NSC (National supercomputer center in Sweden), HIVE supercomputer at SWEGRID, and HELIOS supercomputer provided by UNICC at Chalmers are gratefully acknowledged. The authors wish to thank Professor Squire and Professor Chiu for answering questions related to the experimental work.

## References

- <sup>1</sup>Baker, C., Jones, J., Lopez-Calleja, F., and Munday, J., "Measurements of the cross wind forces on trains," *Journal of Wind Engineering and Industrial Aerodynamics*, Vol. 92, 2004, pp. 547–563.
- <sup>2</sup>Chiu, T. W. and Squire, L. C., "An experimental study of the flow over a train in a crosswind at large yaw angles up to  $90^\circ$ ," *Journal of Wind Engineering and Industrial Aerodynamics*, Vol. 45, 1992, pp. 47–74.
- <sup>3</sup>Copley, J. M., "The three-dimensional flow around railway trains," *Journal of Wind Engineering and Industrial Aerodynamics*, Vol. 26, 1987, pp. 21–52.
- <sup>4</sup>Suzuki, M., Tanemoto, K., and Maeda, T., "Aerodynamic characteristics of train/vehicles under cross winds," *Journal of Wind Engineering and Industrial Aerodynamics*, Vol. 91, 2003, pp. 209–218.
- <sup>5</sup>Hoppmann, U., Koenig, S., Tielkes, T., and Matschke, G., "A short-term strong wind prediction model for railway application: design and verification," *Journal of Wind Engineering and Industrial Aerodynamics*, Vol. 90, 2002, pp. 1127–1134.
- <sup>6</sup>Diedrichs, B., "On computational fluid dynamics modelling of crosswind effects for high-speed rolling stock," *IMechE*, Vol. 217, No. F, 2003, pp. 203–226.
- <sup>7</sup>W. Khier, M. Breuer, F. D., "Flow structure around trains under side wind conditions: a numerical study," *Computers & Fluids*, Vol. 29, 2000, pp. 179–195.
- <sup>8</sup>Diedrichs, B., Berg, M., and Krajnović, S., "Large eddy simulations of a typical European high-speed train inside tunnels," *SAE 2004 World Congress*, SAE Paper 2004-01-0229, Detroit, Michigan, USA, 2004.
- <sup>9</sup>Krajnović, S. and Davidson, L., "Flow Around a Simplified Car, Part I: Large Eddy Simulation, (in press)," *ASME: Journal of Fluids Engineering*, 2005.
- <sup>10</sup>Krajnović, S. and Davidson, L., "Flow Around a Simplified Car, Part II: Understanding the Flow, (in press)," *ASME: Journal of Fluids Engineering*, 2005.
- <sup>11</sup>Krajnović, S. and Davidson, L., "Large-Eddy Simulation of the Flow Around Simplified Car Model," *SAE 2004 World Congress*, SAE Paper 2004-01-0227, Detroit, Michigan, USA, 2004.
- <sup>12</sup>Krajnović, S. and Davidson, L., "Large Eddy Simulation of the Flow Around an Ahmed Body," *2004 ASME Heat Transfer/Fluids Engineering Summer Conference*, Charlotte, North Carolina, USA, 2004.
- <sup>13</sup>Nilsson, H. and Davidson, L., "CALC-PVM: A Parallel Multiblock SIMPLE Multiblock Solver for Turbulent Flow in Complex Domains," Tech. rep., Dept. of Thermo and Fluid Dynamics, Chalmers University of Technology, Gothenburg, 1998.
- <sup>14</sup>Chiu, T. W., "Prediction of the aerodynamic loads on a railway train in a cross-wind at large yaw angles using an integrated two- and three-dimensional source/vortex panel method," *Journal of Wind Engineering and Industrial Aerodynamics*, Vol. 57, 1995, pp. 19–39.